Journal of Materials Processing Technology 214 (2014) 2706–2715

Contents lists available at ScienceDirect

Journal of Materials Processing Technology

journal homepage: www.elsevier.com/locate/jmatprotec

Additive manufactured porous titanium structures: Through-process quantification of pore and strut networks

Taek Bo Kim[a], Sheng Yue[b], Ziyu Zhang[a], Eric Jones[c], Julian R. Jones[a], Peter D. Lee[b,*]

[a] Department of Materials, Imperial College London, London SW7 2AZ, UK
[b] School of Materials, University of Manchester, Manchester M13 9PL, UK
[c] Centre for Materials and Structures, University of Liverpool, Liverpool L69 3GH, UK

ARTICLE INFO

Article history:
Received 16 December 2013
Received in revised form 24 March 2014
Accepted 4 May 2014
Available online 13 May 2014

Keywords:
Additive manufacturing
Selective laser melting
X-ray microtomography
Porous titanium
Quantification methods

ABSTRACT

Titanium and its alloys are successfully used in aerospace through to marine applications. Selective laser melting (SLM) is an additive manufacturing technique, which promises to allow production of novel Ti structures. However, there is still a paucity of accepted methods for quantifying build quality. The viability of using X-ray microtomography (μCT) to quantify and track changes in morphology of SLM Ti porous structures at each stage of the post-laser melting production was tested, quantifying its quality through process. Quantification was achieved using an accessible volume tool to determine pore and strut sizes. Removal of partially sintered struts by cleaning was visualised and quantified. Eighty-eight percent of the struts broken by the cleaning process were found to have connecting neck diameters of less than 180 μm with a mean of 109 μm allowing build criteria to be set. Tracking particles removed during cleaning revealed other methods to improve build design, e.g. avoiding low angle struts that did not sinter well. Partially melted powder particles from strut surfaces were quantified by comparing surface roughness values at each cleaning step. The study demonstrates that μCT provides not only 3D quantification of structure quality, but also a feedback mechanism, such that improvements to the initial design can be made to create more stable and reliable titanium structures for a wide variety of applications.

1. Introduction

Titanium (Ti) and its alloys have been used extensively in many industries due to their low density, high corrosion resistance and oxidation resistance as outlined by Leyens and Peters (2005). More recently, the production of porous structures by additive manufacturing techniques has become more widespread, such as by Davies and Zhen (1983) who outlined several methods of production for foamed metals. In particular, porous Ti structures have been manufactured for use in many applications using a powder metallurgy route which presents a number of advantages, primarily the ability to shape complex structures with tailored mechanical properties at low temperature as shown by Brenne et al. (2013) who studied the microstructure of additive manufactured (AM) porous Ti and its impact on mechanical properties. Of the many AM techniques presented in literature – Dunand (2004) reviewed the production methods of Ti foams by powder sintering and bubble expansion, Wadley (2002) reviewed the development of periodic metallic porous structures and Singh et al. (2010) looked at the AM methods to produce Ti scaffolds for biomedical applications – selective laser melting (SLM) has been found to be a very promising method. This AM approach uses a computer aided design to direct a laser point that melts a powder bed of titanium to directly build Ti structures with controlled porosity. SLM provides a continuous connected pore network that is difficult to achieve using typical foaming methods such as bubble foaming or space-holder foaming, which can form closed pores. SLM allows greater control over the final structure of very complex interconnected strut designs to tailor pore and strut sizes and therefore allows customisation of the mechanical properties of a porous structure.

As SLM is a relatively new technology, it is important to verify and match as-built structures with the original design. This is particularly challenging as AM structures can have complex 3D features that cannot be quantified using normal metrology techniques. Characterisation of porous Ti structures has focused on the microstructure and its bulk mechanical properties. For example, Kobryn and Semiatin (2001) showed how the processing parameters affected Ti microstructure in laser AM Ti foams and Heinl et al.

* Corresponding author at: The Manchester X-Ray Imaging Facility Research Complex at Harwell Rutherford Appleton Laboratory Didcot, Oxon OX11 0FA, UK. Tel.: +44 1235 567789; fax: +44 1235 567799.
E-mail addresses: Peter.Lee@manchester.ac.uk, p.d.lee@ic.ac.uk (P.D. Lee).

http://dx.doi.org/10.1016/j.jmatprotec.2014.05.006

(2008) tailored the elastic modulus of SLM cellular Ti by varying unit cell sizes and laser energy. However it is equally important for morphological characterisation of porous structures to be standardised with proven quality control and assurance technologies, especially as porous structures can be customised and changed easily to tailor its properties. Therefore, there is a great need for the ability to track the development of these porous structures not only within batches (quality control) but the same structure throughout a production lifecycle (quality assurance). This is particularly relevant as potentially un-melted and loosely connected Ti particles need to be removed from the structure before use.

One such method to clean structures is to administer abrasive jet blasting using sublimating pellets. Sintering is then applied to enhance the mechanical properties of the scaffolds by homogenising the strut diameters. The rationale for using such a cleaning procedure is to reduce the risk of contamination in the porous structure and there is also the potential to eliminate a drying cycle. Sherman (2007) reviews the key parameters in jet blasting which make such a technique widely accepted in industry. In particular, Masuda et al. (1994) optimised cleaning parameters for improved efficiency using a model based on jet theory, whilst Liu et al. (2011) assessed jet blasted surfaces by high-speed microscopes to track the removal of contaminants on a surface, exemplifying the development of jet blasting. However, these studies have mainly focused on the removal of organic contaminants rather than powder particles and the effectiveness of jet-blasting, whilst there has not been enough study on jet blasting's influence on final build quality. Further, studies have been restricted to measuring surface quality of a bulk piece, not a porous 3D structure such as the ones used in this study.

To study morphological changes, X-ray microtomography (μCT) can be used as a non-destructive method to examine individual structures. Kerckhofs et al. (2008) used μCT to validate the use of SLM manufacture of porous structures with the current gold-standard of using histology and have shown that within error, μCT tomograms can be used to validate structural features of porous Ti. Further to this, Van Bael et al. (2011) used μCT to study the as-built porous Ti structures built via SLM to its design parameters and showed good repeatability in production but showed that the final products could be very different from the original design. Van Bael's study acts as a good precursor for our current study which applies the work further by quantifying the changes during the process lifecycle of porous Ti structures, not just to its CAD design.

Combined with three-dimensional (3D) visualisation using μCT, a number of quantification tools have been developed to study pore sizes in different materials. Mangan and Whitaker (1999) introduced the distance transform and watershed algorithm, which provided a good basis to segment an interconnected spherical pore structure from a μCT scan. Atwood et al. (2004) then showed how spherical pore and interconnect sizes can be quantified. An experimental approach to measuring pore size is by using mercury intrusion porosimetry (MIP). However, MIP is a destructive method and calculates the constriction of mercury intrusion, which approximates to interconnect (area shared between conjoined pores) sizes more than the actual pore sizes. A validation of MIP results of open spherical pores sizes measured from μCT quantification via watershed was carried out by Jones et al. (2007). However for SLM-manufactured porous Ti structures, which have a channel-like pore network, a medial axis approach is more appropriate than estimating to spheres. The minimal ball approach to quantify pore size in channels as shown by Ngom et al. (2011) or approximation of channel space as simple volumes as shown by Monga et al. (2007), can be successfully applied not only to pores but also to strut thicknesses.

This study aims to develop methods of quantifying AM components together with μCT and applying this to study the effects that jet blasting and sintering may have on the morphology and shape of porous structures and quantifying these changes. The quantification tools to characterise pore and strut size distributions, and the ability to track morphological changes in the same sample throughout its manufacturing life-cycle via μCT is outlined in this paper. Using μCT, it is possible to non-destructively image the structure of the scaffolds in 3D and identify defects to assess quality and also acts as a feedback tool to continuously update and improve designs.

2. Materials and methods

2.1. Production and cleaning of irregular porous titanium structures

SLM was used to build Ti structures with 60 and 75% porosity levels (termed S60 and S75 respectively). The component design was defined in a 3D CAD model using Pro Engineer software (Creo Elements Pro, PTC, Needham, MA) and represents a portion of a specimen which is to be manufactured in a porous form. This portion is then populated with predetermined unit cell geometry (octahedrons) which are also tessellating. These structures were then subjected to distortion by perturbation of its Cartesian coordinates which represent the spatial location of the vertices of the strut members that form the octahedron. This is to modify the appearance and structural properties of the unit cells to create a random appearance; it also provides a very complex structure ideal for testing the robustness of quantification algorithms.

The SLM fabrication process develops in a layer wise fashion, with the laser beam creating a series of melt spots on the powder bed that correspond to the build files created from the CAD model, thereby forming a small slice of the cellular structure. The Ti powders used were highly spherical, gas atomised grade 1 and had a diameter between 0 and 45 μm, with a modal diameter of 28.5 μm (Sumitomo Corp., Tokyo, Japan). Subsequent powder layers of 50 μm are deposited and laser scanned until the parts are built, with the process taking place in an argon atmosphere to prevent oxidation. The laser power was set at 2253 W and the exposure time for each spot was 300 μs.

Six cylindrical specimens of diameter 25.4 mm (1″) and height 7.5 mm (top 1.2 mm is porous) were fabricated for each sample set, S60 and S75, and embedded with three solid fiduciary markers to assist image registration. Excess powder was removed and recouped by blowing with argon gas. The as-built samples were scanned by μCT at two resolutions as described later (termed *as-built*).

The effect of a jet blasting process was then investigated. The samples were cleaned through vigorous jet blasting using pellets that sublimate on impact, before being placed in an ultrasonic wash of Micro-90 (Sigma-Aldrich Corp., St. Louis, MO) solution. A series of rinses using de-ionised and distilled water was used to further remove any powder trapped within the parts. The samples were scanned by μCT again after this step (termed *cleaned*).

Once cleaned, the porous structures were put through a sintering process in high vacuum. The samples were set at 100 °C for 30 min before being heated at a ramp rate of 7.5 °C/min to 900 °C and held for 3 h to sinter. The samples were scanned a third time by μCT after sintering (termed *sintered*).

Test porous pieces were included on the build plate in order to characterise the porous designs post-production in terms of its porosity by the gravimetric method and compressive strength (Instron, Norwood, MA).

In this study, the following sequences in the build process are defined:

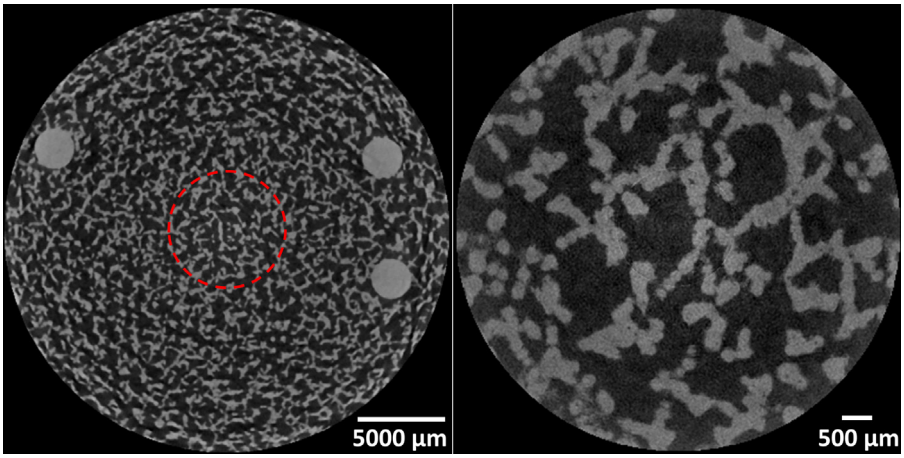

Fig. 1. XY slice of sample at (A) 27 μm/voxel resolution (full scan) and at (B) 7.5 μm/voxel resolution (local scan). The region in the red circle is the area from the full scan that is reconstructed at higher magnification in the local scan. (For interpretation of the references to colour in this figure legend, the reader is referred to the web version of the article.)

- A strut is composed of a number of melt points (*point nodes*) created in an oblique direction over six powder layers of 50 μm thickness.
- A *strut node* is formed by the convergence of four struts which correspond to the profile of an upper or lower portion of a regular or irregular wire-frame octahedron.

2.2. Tomography

Micro-CT scans were performed using a laboratory based μCT facility (nano-focus, Phoenix|x-ray General Electric Company, Measurement and Control) with an accelerating voltage of 100 kV and current of 70 μA, and 0.5° angular rotation interval. A 0.5 mm thick copper filter was also placed between the sample and the X-ray source to reduce beam hardening artefacts as explained by Stauber and Muller (2008). Seven hundred and twenty projections across 360° were acquired per scan, with three 1600 ms projections averaged per angle to minimise noise.

Due to the trade-off between the sample size and the spatial resolution in normal μCT imaging, each specimen was first scanned at a voxel size of 27 μm (full scan) so that the entire sample was kept within the field-of-view during the 360° rotation. Then the sample was moved closer to the X-ray source to obtain a higher resolution of 7.5 μm/voxel (local scan). In order to reconstruct the central part of the sample at high resolution, local tomography was used which enables the reconstruction of an object despite it not being fully inside the field-of-view (FOV). This is an important technique that allows scanning at higher resolutions in exchange for poorer signal-noise ratio. Local tomography works best in porous cylindrical samples where the attenuation from material outside the FOV is roughly equal at all projections. The details of the local tomography technique can be found in Kyrieleis et al. (2011).

2.3. Quantitative analysis of μCT images

2.3.1. Image processing and registration

The reconstructed images were passed through a $3 \times 3 \times 3$ median filter in order to reduce the noise in the scans. To minimise the effect of beam hardening artefacts that occur in the reconstructions, a radial mask was applied to normalise the intensity values. The circular mask was graded from the centre to the outside such that the effect of brighter than expected values at the edges would be minimised.

μCT images of the same sample obtained at different stages and by different imaging settings (i.e. full scan and local scan) were numerically aligned with image registration. Initially, three fiducial markers were used to align the images of the same sample. Then an iterative optimisation algorithm, using coarse re-sampling of data towards finer resolutions was applied for accurate image registration as discussed by Pluim et al. (2000). The full and registered local scans are compared in Fig. 1.

Once registration was complete, it was possible to visualise the difference between the volumes based on their greyscale (from its x-ray attenuation). The adhered material that was removed from the cleaning step was isolated and characterised. Changes in strut morphology were also characterised after sintering. In order to find the connecting neck sizes of partially melted particles, the particles were dilated to find the area in contact with its corresponding strut. The resulting diameter of this interconnect region was measured using a principal component analysis based method presented in detail by Yue et al. (2011). This method calculates the principal axes of an object from the eigenvectors of a covariance matrix based on the Cartesian co-ordinates of all of the voxels that make up the object. From this, the length of the object is taken as the length along its major axis.

2.3.2. Pore size distribution

The reconstructed images require thresholding prior to quantification. Global thresholding from the histogram, developed by Otsu (1979), was used to differentiate pore and material. In each scan, the threshold was determined using the mid-point value between the two peaks in the greyscale histogram. Pore size distribution of the samples was estimated using an '*accessible volume*' algorithm as described by Yue (2010). The accessible volume algorithm required the data to be binarised into two phases (Struts = 1, pores = 0). Accessible volume uses a set of testing spheres of given radii that measures the volume filling of the segmented space.

The change in accessible volume per testing sphere was plotted and the normalised median value and modal values were both taken to represent the distribution. The full scan data was used to find the pore size distribution as this considers a greater representative volume than the local scan and therefore shows a more truly representative pore distribution of the entire sample. Porosity was estimated by calculating the fraction pore volume over the total volume.

2.3.3. Strut size distribution

Accessible strut volume and size distribution were estimated using the same algorithm as in Section 2.3.2 but applied to the struts. The local scan data was used to measure the strut sizes as the

higher resolution was required to differentiate the small changes in strut thickness. Comparable strut distributions were compiled by more conventional methods such as manual measurement of strut thicknesses from SEM images. Manual measurements from μCT reconstructions were also taken. This was done by measuring the perpendicular width of struts in a 2D slice to the strut length as seen in Fig. 3b and d. 40–75 measurements were taken for each distribution for each porosity: S60 and S75; and each cleaning state: as-built, cleaned and sintered.

2.4. SEM imaging

The samples were scanned using secondary electron imaging using the JSM 5610 LV (Variable Pressure SEM JEOL) with an accelerating voltage of 20 kV and a 15 mm working distance.

2.5. Sampling and statistics

As each process in the cleaning and sintering procedure can have variable effects on the Ti structures, six samples produced using the identical design for each porosity were analysed. Each of the six samples was put through the same process of cleaning and sintering and μCT was performed at every step. Detailed analysis using accessible volume was applied to three of the six samples. Due to the huge amount of data obtained, the results shown in this study are from a typical representative sample of S60 and S75. The field-of-view for the high resolution (7.5 μm/voxel) scans were limited by the size of the detector and therefore is only a selective view of the centre of the entire sample.

3. Results

3.1. Porosity and reconstruction

Initial characterisation showed that the porosity of the built structures (65 ± 2%) matched closely to its target porosity (65%) when tested gravimetrically. The compressive strength was found to be 42 ± 4 MPa.

A typical 2D slice through the sample obtained from the μCT scan reconstruction is shown in Fig. 1: for the low (Fig. 1a) and high (Fig. 1b) resolution scan.

The mean porosities of the samples at each process step are given in Table 1. The average porosities measured match the design targets closely. The lower resolution (full scans) tended to give a lower apparent porosity than the higher resolution scans by about 5%, due to the large voxel size over-estimating strut thickness.

3.2. Pore size and strut size distributions from accessible volume

Fig. 2a–c shows the pore size distributions as quantified using the accessible volume algorithm from volumes with a 27 μm voxel size. The graph plots the change in accessible volume as a function of the pore diameter. A large change in accessible volume correlates to a larger proportion of pores constricted at this diameter. Fig. 2a shows the pore distribution of a representative cleaned samples for the different porosity levels, S60 and S75. The median/modal values for the S60 and S75 samples are 287/292 μm and 326/426 μm, respectively. The median values are given as they fully illustrate changes in distribution skew and representative diameter through processing (see Table 2).

Fig. 2b shows the pore size distribution of a S60 sample at each stage with the median values in Table 2. For S75 sample, the modal values were higher than the S60 sample at 426 μm; however a small peak at 292 μm were also observed in some samples as shown in Fig. 2c. The local scans were not used to find the pore size distribution, as the sampling volume was too small to give a representative

Table 1
Mean porosity determined by analysis from micro-CT 3D reconstruction volumes of porous titanium structures.

Cleaning stage	Actual porosity (%)			
	60% target		75% target	
	Full	Local	Full	Local
Original	55.3 ± 0.6	61.3 ± 1.1	64.8 ± 0.4	69.2 ± 2.1
Cleaned	57.7 ± 0.2	62.2 ± 1.3	66.9 ± 0.5	71.5 ± 0.2
Sintered	56.7 ± 1.1	65.4 ± 0.5	66.4 ± 1.4	69.8 ± 1.4

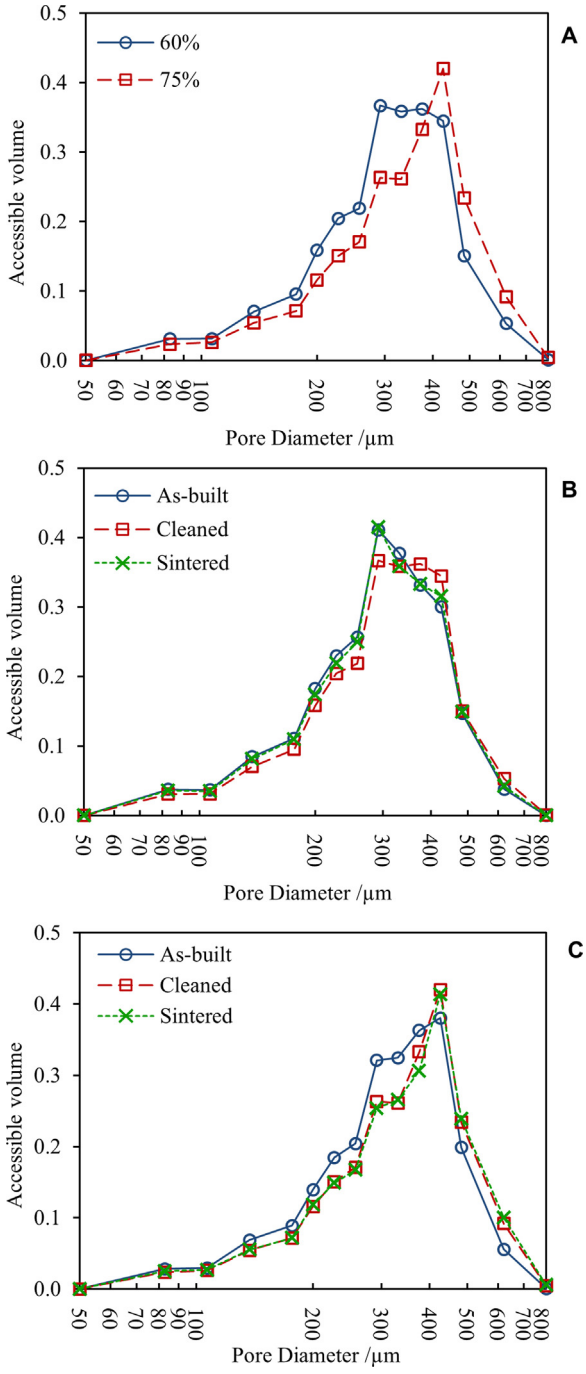

Fig. 2. Accessible volume method to find pore size distributions of (A) cleaned S60 and S75 samples; and (B) after each stage in the procedure as-built, cleaned and sintered for S60 sample and (C) in a S75 sample. The resolution used was 27 μm/voxel.

Table 2
Median pore and strut sizes from accessible volume for 60 and 75% porosity foams at each processing stage. Values are obtained from scans at two different resolutions – 27 μm/voxel for full scan and 7.5 μm/voxel for local scan (Note: error is variability between samples).

Porosity	Cleaning stage	Median pore size (μm)		Median strut size (μm)	
		Full	Local	Full	Local
60%	Original	283 ± 1.4	276 ± 6.0	235 ± 3.2	226 ± 7.1
	Cleaned	296 ± 1.0	279 ± 1.6	230 ± 0.6	231 ± 12
	Sintered	292 ± 5.3	314 ± 7.8	236 ± 3.3	231 ± 3.2
75%	Original	308 ± 1.7	283 ± 8.0	193 ± 2.1	189 ± 9.7
	Cleaned	328 ± 1.8	303 ± 1.5	191 ± 1.5	191 ± 2.9
	Sintered	317 ± 7.6	302 ± 5.6	183 ± 8.8	198 ± 10

distribution of the entire sample. The differences in pore size distributions are small, although the greatest difference is between the uncleaned state and the cleaned step as this is the most aggressive procedure.

Fig. 3a shows a SEM image of a region of a S60 at 35× magnification. Reconstruction of the μCT images as shown in Fig. 3c can be visually correlated with the SEM images. The point nodes can be more clearly defined in the SEM images, whilst the quality of the μCT image is voxel size dependent. Fig. 3b and d shows the comparison of the same strut. The μCT strut shows a much smoother surface than the SEM image. The manual measurements from the SEM images and μCT images are compared to the strut size distributions obtained by accessible volume in Fig. 4d.

Fig. 4 shows the strut size distributions of representative samples comparing both porosities (Fig. 4a) and at each cleaning step (Fig. 4b and c). Again, the difference in strut size between S60 and S75 samples were as expected, with the S60 having overall thicker struts. Both porosities measured by accessible volume had thicknesses close to the target thickness of 180 μm. The S60 sample showed modal values of 188 μm and a smaller peak at 274 μm. The median value was found to be 227 μm. The S75 sample showed modal value of 155 μm and a median value of 201 μm. There was no defining peak found using the accessible volume algorithm, but 86% of the strut volume change occurred in the range of 129–331 μm for the S60 sample and in the range 129–274 μm for the S75 sample.

Fig. 4b shows the strut distribution after each step from accessible volume of a S60 sample. It shows that there was only a small change in the strut sizes, but there was a marked reduction in the fraction of 188 μm struts in the cleaned sample. The median values for as-built, cleaned and sintered samples were 218, 245 and 227 μm respectively for this sample, but the variance between samples measured showed that these differences were not significant. The apparent increase in the median value of the cleaned sample is due to the lower fraction of 188 μm struts. The struts showed two peaks at 188 and 274 μm.

Fig. 4c shows the S75 strut distribution from accessible volume algorithm. From the graph, the fraction of thinner struts (from 50 to 129 μm) has decreased for the cleaned and sintered samples. The sintered sample also showed a drop in the 274 μm peak, as the sintering smoothens rougher struts. This is reflected in the median values for as-built, cleaned and sintered samples (Table 2).

Fig. 4d compares the S60 strut distributions after cleaning and sintering, measured using three different techniques. First is using the accessible volume algorithm, a specific code to measure the strut thickness based on its distance map; secondly is manual measurements from SEM and lastly from manual measurements from 3D reconstruction of μCT images. Fig. 3b and d shows the measurement of a typical strut in SEM and μCT reconstructions. Despite the large number of measurements taken from SEM and μCT images, these tended to give a narrower distribution than from the accessible volume algorithm. The modal values of strut size from the accessible volume algorithm, SEM and μCT measurements were all found to be 187 μm. SEM measurements were also able to show a

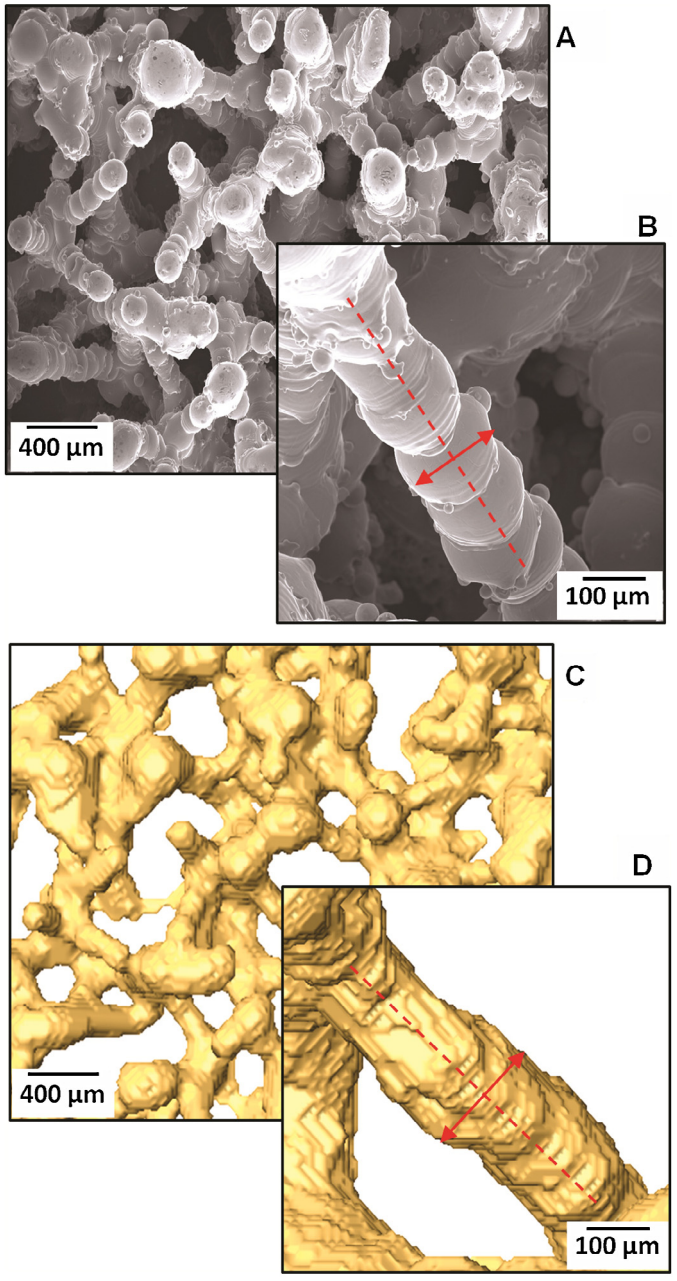

Fig. 3. (A) Shows a SEM image taken at ×35 magnification of a cleaned and sintered S60 sample showing the strut network, with the strut and point nodes being clearly identifiable. (B) Shows a SEM image at ×150 magnification of an individual strut. The diameter of the strut (in red arrows) was measured as the perpendicular thickness from the centre line of the strut (dotted red line). (C) Shows the μCT reconstructed 3D image of the same area as (A), voxel size is 27 μm. (D) Shows the diameter manually measured from μCT. (For interpretation of the references to colour in this figure legend, the reader is referred to the web version of the article.)

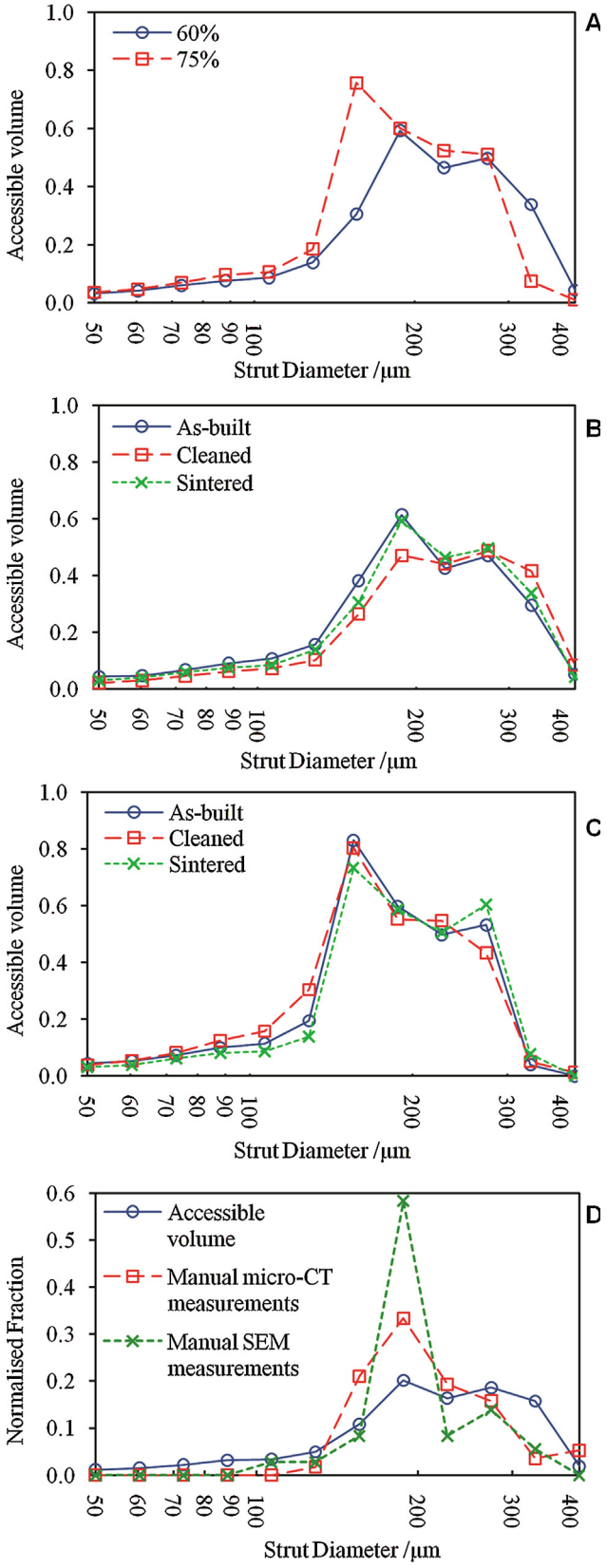

Fig. 4. Strut size distributions measured from accessible volume for (A) Two cleaned samples of different porosities 60 and 75%; (B) shows the strut size distributions at each stage during the cleaning process for a S60 sample; (C) shows the strut size distribution for a S75 sample. (D) Shows the comparison of strut size distributions of sintered S60 samples obtained by 3 different methods: accessible volume, manual 3D measurements of μCT reconstructions and manual measurements from SEM images.

second peak at 274 μm which was also present from the accessible volume distribution.

3.3. Jet blasting and strut removal

Jet blasting is a common method of abrasive method of cleaning. It is used to remove unwanted particles left over that may be partially melted onto struts. In order to quantify its effects using μCT, the scans must be registered before and after cleaning. Fig. 5a shows the 3D reconstruction of a S60 sample with the parts of the strut that were removed or bent by the cleaning highlighted in red, scanned at 27 μm/voxel. The unaffected struts are shown in yellow. The volume of material that was affected was less than 3% (2.4 ± 0.5%) for S60. The affected struts were spread evenly across the surface, but struts nearer the surface were more likely to have particles removed or bent. The number of affected particles in the ROI was 450, of varying sizes between 30 and 475 μm. The average size of neck diameter of the removed particles in this ROI was found to be 109 ± 56 μm. 88% of the connecting neck diameters were less than 180 μm, which was the target strut size.

Using a large voxel size was necessary to analyse a statistically significant volume, however to quantify the neck sizes accurately, the local scan (7.5 μm per voxel) was used. Fig. 5b shows a small area where particles are removed. The particles have a diameter similar to the thickness of the struts (200 ± 20 μm) and have connecting neck diameters of 97 μm ± 22 μm as found by principal component analysis. Fig. 5b–d shows the removed particles in dark orange from the struts. Fig. 5e shows the particles from an *X*–*Z* viewpoint, from which the angle the line of particles makes with the *X*–*Y* plane was found to be 6.06°.

Fig. 6 shows struts at each stage of the cleaning process (A – as built, B – cleaned, C – sintered) showing the removal of small partially melted powder particles. These particles can only be resolved at the higher resolution of 7.5 μm/voxel due to their small size. The red arrows highlight the powder particles that have been removed from the as built strut to the jet-blasted strut. S_a, the areal surface roughness defined as the arithmetical mean height of the surface, was found to be 11.0 ± 4.1 μm for the as-built strut, 10.6 ± 3.8 μm for the jet-blasted strut and 10.8 ± 3.8 μm for the sintered strut. The strut thicknesses match the target strut thickness which was a radius of 90 μm. The error values correspond to the accuracy of the polar co-ordinates of the strut surface, which was accurate to within ± 0.5 voxel.

Fig. 7 shows examples of individual strut bending after each process. After registration of the samples, struts that are bent can be easily identified. The bending occurs at the surface of the samples which are in direct contact with the blasting. Fig. 7a and b shows deformation before cleaning (in yellow) and after cleaning (shown in green), which is the step that exhibits the majority of deformation. Fig. 7c shows deformation of a strut before sintering (in green) and after sintering (in purple). Such examples of deformation are much rarer in the post-sintering case than the post-blasting case.

4. Discussion

4.1. Tomography

Acquiring 3D tomography scans can give high quality images of the volume, but it is much more difficult to obtain information regarding its properties. In order to quantify changes in the titanium, it is necessary to threshold the images. Thresholding is an inherent difficulty in μCT due to noise and reconstruction artefacts and has been previously discussed by Koseki et al. (2008) and Stauber and Muller (2008) in greater detail. At lower resolutions, the error in thresholding can lead to large differences in

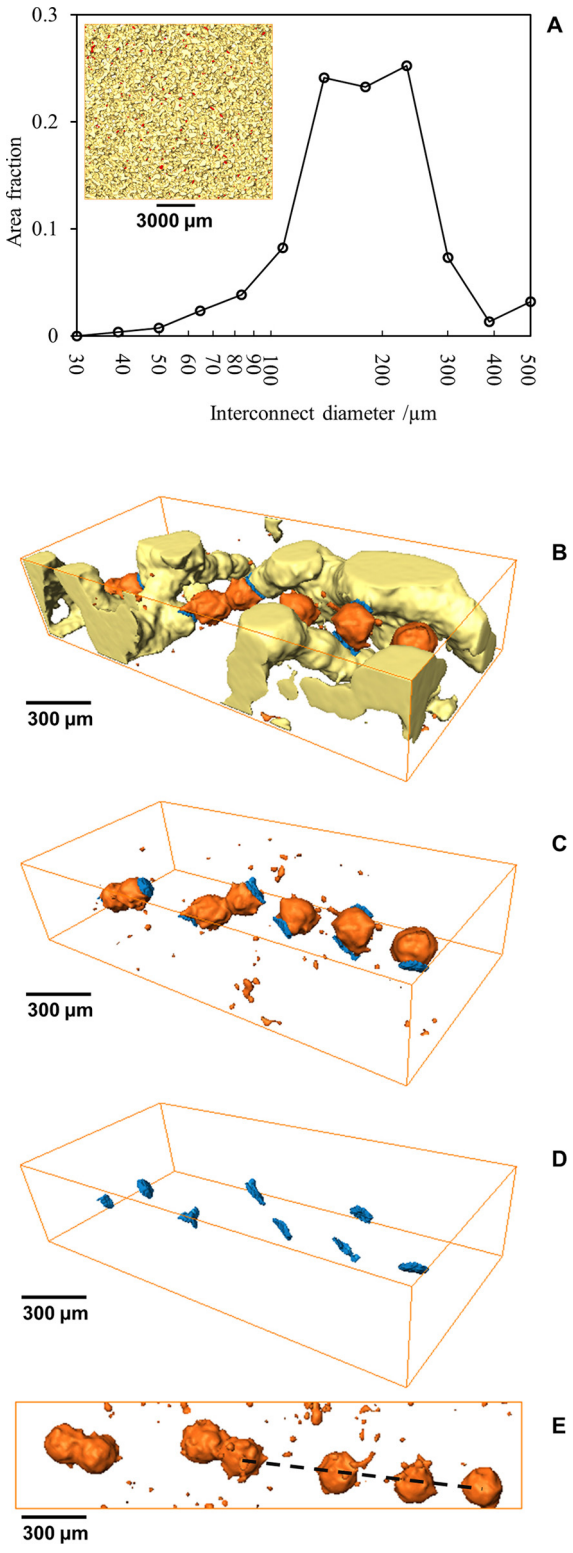

Fig. 5. (A) Shows the interconnecting neck diameter distributions of strut particles that have been removed during the blasting step for a S75 samples. Inset is a reconstruction of a small volume of the structure (27 μm/voxel) where the titanium struts are shown in yellow and the particles that were removed highlighted in red. (B–D) Shows a progression of images that show how the interconnecting neck diameters were found. In (B), the titanium struts are shown in yellow. The dark-orange spherical particles are particles of the original titanium network that were broken off during blasting. (C) and (D) show the individual particles and their neck interconnects which are shown in blue. E: shows the low angle struts that could be removed from the design prior to production. The scale bar shows 300 μm. (For interpretation of the references to colour in this figure legend, the reader is referred to the web version of the article.)

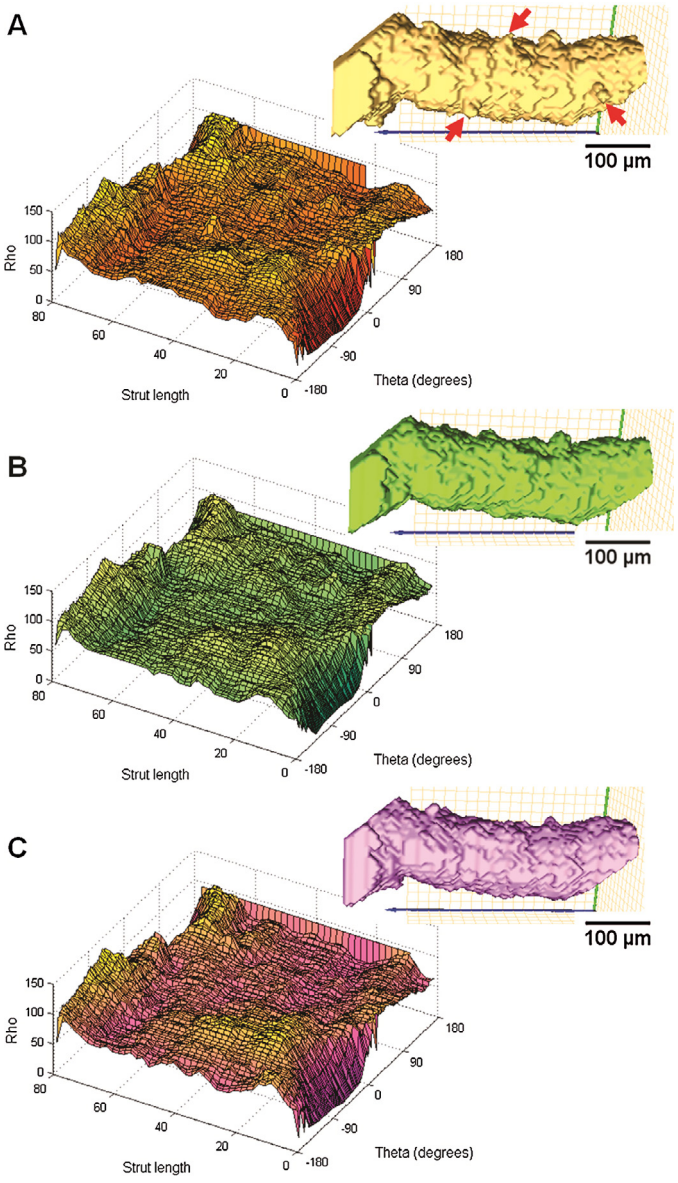

Fig. 6. Shows the surface profiles of a typical strut shown inset scanned at 7.5 μm/voxel resolution. Rho is the height of the surface from the centreline of the strut, strut length and theta are the components of the polar co-ordinates of the strut. (A–C) Compares the same strut at as-built, cleaned and sintered stages respectively. (For interpretation of the references to colour in text, the reader is referred to the web version of the article.)

measurements. Since the intensities of each scan changes from scan to scan, the threshold value was found for each scan using its histogram. The values of the pore space and titanium peaks provide a reliable, objective and repeatable way of finding a threshold value.

4.2. Accessible volume

The accessible volume theory is used as a method to quantify the pore and strut sizes by comparing the volume filled by spheres of increasing radius. The use of previous techniques is not adequate or appropriate for the pore shapes found in SLM-manufactured structures as they are not spherical pores as in Jones et al. (2009) and others previously mentioned. Accessible volume theory produces a distance map from the struts towards the centre of the pore and assigns whether or not a sphere of a given diameter is able to occupy that space as long as it is connected to pores on the surface. As the

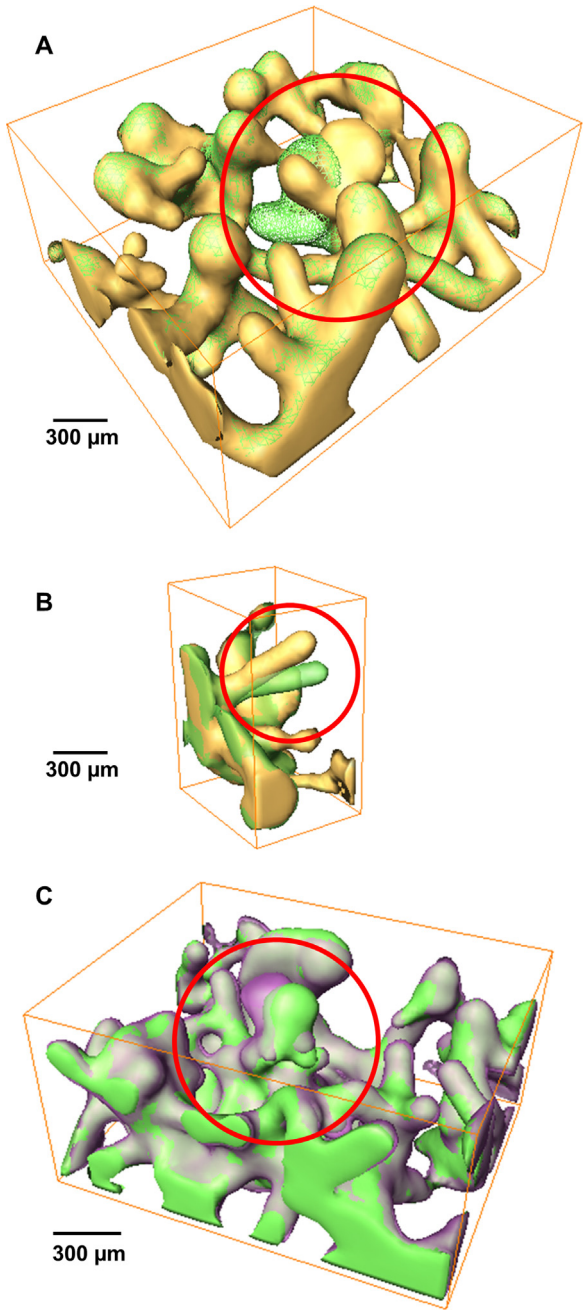

Fig. 7. Three examples of bending found by the comparison of registered samples (A–B) before (in yellow) and after (in green) blasting and (C) before (in green) and after (in purple) sintering. Region of deformation is shown in red circles. The scale bar shows 300 μm. (For interpretation of the references to colour in this figure legend, the reader is referred to the web version of the article.)

radii of the spheres increase, pore spaces that are smaller or have an interconnect size less than this, cannot be filled and therefore leads to a smaller volume being filled. The pores must be linked to the outer face of the sample, such that it measures the volume that the testing sphere can cover. In this way, accessible volume algorithm is analogous to the pore size distribution calculated by changes in pressure in MIP.

The pore size distributions from the accessible volume algorithm showed similar variance in the S60 and S75 samples, although the S75 sample shows a positive skew due to the larger pore diameters. For the strut size distributions, the S60 samples have positive skew. The smaller peaks seen at 274 μm in the SEM and accessible volume strut distributions are representative of the larger strut nodes that form due to the convergence of struts. Furthermore, the modal values of strut size from accessible volume, SEM and manual μCT measurements were all found to be 187 μm. This correlates well with the initial target strut diameter which was 180 μm (Fig. 4d).

It is interesting to note that there was very little difference seen between the pore size distributions at each cleaning stage (Fig. 2). This means that overall; there is little change in the macro-structure when the samples undergo this cleaning process. This lends to the assumption that these cleaning and production methods do not change the inherent pore and strut sizes. The accessible volume method is able to differentiate the pore and strut sizes of two samples of different porosities, which means it is sensitive to manufacturing design and reflects such differences. The resolution was also an important factor in the quantification as larger voxel sizes (27 μm in this case) were found to overestimate the size of the struts, leading to generally lower porosities and pore sizes. When measuring strut size, the median values of the struts were seen to increase from as-built to cleaned. It would be expected from blasting for material to be removed and therefore the strut size should show a decrease in the strut size. However, with the removal of thin struts, the accessible volume of struts shifts to the right to reflect the larger fraction of thicker struts that was not removed.

As the nature of the manufacturing method of these structures produces uneven and globular struts, the measuring strut and pore sizes are difficult using conventional methods. A problem when measuring the strut diameters from SEM and even from μCT reconstruction images is that the struts are not of uniform diameter across its length. This means that manual measurements from images are based on measurements that are considered a representative length of the strut can be prone to bias. This leads to the narrow distribution, but similar modal values as seen in Fig. 4. The accessible volume method considers all the thicknesses in each strut and pore, which provides information about the proportion of small, constricting interconnects.

4.3. Quantification of effect of cleaning

By using SLM, it is possible to reproduce almost identical structures repeatedly by using the same design. However, there are potential problems related to SLM such as partial melting of powders and trapped powder. Xue et al. (2007) fabricated porous Ti structures using a similar additive layer manufacturing method like SLM termed laser engineered net shaping (LENS). These cellular materials had a pore size range of 100–700 μm and a widely varying porosity of 17–70%, but contained partially sintered Ti particles which could lead to reduced wear and fatigue properties.

In order to find the connecting neck diameter distribution, a significant number of necks were required. The particles that were removed from blasting were found to have spherical morphology with a diameter similar to the strut diameters measured by accessible volume. This suggests that the particles that are removed are not particles from the melting process, but are more likely to be struts that have broken off as a result of the cleaning process. Struts with thin necks are a result of individual point nodes within the strut being too far away from its adjacent neighbours, when the strut with a low angle is formed. This however, can be easily resolved by modifying the initial design files such that struts that form low angles – and are therefore more likely to have thin necks – are removed. This observation is clearly illustrated in Fig. 5 as a string of disconnected fragments. In 3D, these particles look largely spherical in shape and it is clear that these fragments are components of a strut (individual laser melt spots) that have possibly broken off due to weak connecting necks (highlighted in blue).

Jet blasting and subsequent sintering removes particles that would be liable to becoming loose if they had been implanted into the body. From Fig. 5a, it can be seen that struts with sub-optimal thickness (88% of connecting neck diameters were less than the target strut thickness), are most likely to be removed during cleaning. It is also important to note that μCT is able to detect the changes in structure of individual struts whereas this would be difficult to achieve from SEM or other conventional methods used to quantify these structures. It is also not possible to separate the different substituent parts as in Fig. 5b–d in SEM and thus quantifying these neck sizes would be impossible.

Local scans (voxel size 7.5 μm) are required to visualise the removal of powder that have been partially melted onto the struts as opposed to large scale strut particle removal seen in the full scans. As seen in Fig. 6, the struts before and after cleaning show signs of powder particles being removed at the positions indicated by the arrows. Qualitatively, the cleaned strut is smoother which means that there is a reduced chance of partially melted powder particles breaking off. When this change is characterised quantitatively by S_a, the areal surface roughness, it can be seen that the standard deviation of the struts are lower for the cleaned strut (10.6 ± 3.8 μm) than the as built strut (11.0 ± 4.1 μm), although there is no statistical significance in the difference. The quantitative values of S_a are not conclusive of cleaning having a positive effect on powder removal, however, when considered in association with the qualitative observations, it appears that powder is being removed from the strut surface and thus lowering the strut roughness.

As is the case for most μCT scans, the trade-off between spatial resolution and sample size means that often detail is lost in order to accommodate a greater sample size. For example, in this study, the lower resolution scan at 27 μm voxel size was used to quantify the neck diameter distribution. This means necks of less than 27 μm were not measured and the sensitivity of the results was reduced when the features themselves are less than 100 μm. Additionally, scanning titanium also leads to beam hardening and these effects also impair image quality and therefore reduces the effective resolution. In this study, the use of dual-resolution scanning and registration minimises themeasurements error.

4.4. Qualitative observations of the effects of the cleaning procedure

An unintended effect of the cleaning procedure was observed in the form of strut bending. The bending of struts on the surface of the samples could only be made by visual inspection after accurate registration of the samples.

Although the jet blasting technique is primarily used for the removal of unmelted titanium powder on the strut surface, the abrasive technique may also cause deformation of the structure which can lead to strut bending. The regions that were most affected were struts near the surface, which were in closer proximity with the blast media. As seen in Fig. 7a and b, struts that are not connected to a central node (i.e. unsupported struts) are more likely to bend than struts that are connected. Bending of struts can lead to a possible reduction in the strength of the strut, thus making it more likely to break. It is proposed that by modifying the initial computer design to make all struts on the surface end in a node, the number of bending occurrences from jet-blasting can be reduced. Fig. 7c illustrates a case of bending that was found before and after sintering.

5. Conclusions

Jet blasting and sintering of the structures produced by SLM leads to localised removal of partially adhered Ti powder and weak struts. This process does not affect the macro-properties of the overall pore or strut network, indicating that the cleaning process does not change the original computer aided design of the structure and its porosity. Micro-CT is able to track and quantify these changes to the porous structure in a non-destructive manner progressively through the 3 stage process and using the same sample. Such an analytical procedure is a powerful tool and may be applicable to quality control procedures. The resolution of μCT scans is an important factor in the accuracy of the quantification of pore and strut sizes; the 7.5 μm voxel size used in this study was sufficient to find struts that had been broken off and also powder particles that were removed during the cleaning process. The ability to register large volumes in 3D, allows the observation of the physical effects of cleaning such as bending. From these observations, modifications in the design phase can lead to direct and effective improvements in the end-product such as node-terminating struts and the removal of potential low-angle struts. The 3D images offered by μCT give unique advantages from visualisation of direct changes to porous structures, and for quantifiable datasets which can be used to improve structure designs, that are not available using conventional 2D techniques.

Acknowledgements

We would like to acknowledge the assistance provided by the Manchester X-ray Imaging Facility, which was funded in part by the EPSRC (grants EP/F007906/1, EP/F001452/1 and EP/I02249X/1) and the Research Complex at Harwell.

References

Atwood, R., Jones, J., Lee, P., Hench, L., 2004. Analysis of pore interconnectivity in bioactive glass foams using X-ray microtomography. Scr. Mater. 51, 1029–1033.
Brenne, F., Niendorf, T., Maier, H.J., 2013. Additively manufactured cellular structures: impact of microstructure and local strains on the monotonic and cyclic behavior under uniaxial and bending load. J. Mater. Process. Technol. 213, 1558–1564.
Davies, G.J., Zhen, S., 1983. Metallic foams: their production, properties and applications. J. Mater. Sci. 18, 1899–1911.
Dunand, D., 2004. Processing of titanium foams. Adv. Eng. Mater. 6, 369–376.
Heinl, P., Körner, C., Singer, R.F., 2008. Selective electron beam melting of cellular titanium: mechanical properties. Adv. Eng. Mater. 10, 882–888.
Jones, J.R., Poologasundarampillai, G., Atwood, R., Bernard, D., Lee, P.D., 2007. Non-destructive quantitative 3D analysis for the optimisation of tissue scaffolds. Biomaterials 28, 1404–1413.
Jones, J.R., Atwood, R., Poologasundarampillai, G., Yue, S., Lee, P.D., 2009. Quantifying the 3D macrostructure of tissue scaffolds. J. Mater. Sci. Mater. Med. 20, 463–471.
Kerckhofs, G., Schrooten, J., Van Cleynenbreugel, T., Lomov, S.V., Wevers, M., 2008. Validation of X-ray microfocus computed tomography as an imaging tool for porous structures. Rev. Sci. Instrum. 79, 013711.
Kobryn, P.A., Semiatin, S.L., 2001. The laser additive manufacture of Ti–6Al–4V. J. Min. Met. Mater. Soc. 53, 40–42.
Koseki, M., Hashimoto, S., Sato, S., Kimura, H., Inou, N., 2008. CT image reconstruction algorithm to reduce metal artifact. J. Solid Mech. Mater. Eng. 2, 374–383.
Kyrieleis, A., Titarenko, V., Ibison, M., Connolley, T., Withers, P.J., 2011. Region-of-interest tomography using filtered backprojection: assessing the practical limits. J. Microsc. 241, 69–82.
Leyens, C., Peters, M., 2005. Titanium and Titanium Alloys: Fundamentals and Applications. Germany: DLR-German Aerospace Center, pp. 513.
Liu, Y.-H., Maruyama, H., Matsusaka, S., 2011. Effect of particle impact on surface cleaning using dry ice jet. Aerosol Sci. Technol. 45, 1519–1527.
Mangan, A., Whitaker, R., 1999. Partitioning 3D surface meshes using watershed segmentation. IEEE Trans. Vis. Comput. Graph. 5, 308–321.
Masuda, H., Gotoh, K., Fukada, H., Banba, Y., 1994. The removal of particles from flat surfaces using a high-speed air jet. Adv. Powder Technol. 5, 205–217.
Monga, O., Ndeye Ngom, F., François Delerue, J., 2007. Representing geometric structures in 3D tomography soil images: application to pore-space modeling. Comput. Geosci. 33, 1140–1161.
Ngom, N.F., Garnier, P., Monga, O., Peth, S., 2011. Extraction of three-dimensional soil pore space from microtomography images using a geometrical approach. Geoderma 163, 127–134.
Otsu, N., 1979. Threshold selection method from gray-level histograms. IEEE Trans. Syst. Man Cybern. 9, 62–66.
Pluim, J., Maintz, J., Viergever, M., 2000. Image registration by maximization of combined mutual information and gradient information. In: Delp, S., DiGoia, A., Jaramaz, B. (Eds.), Medical Image Computing and Computer-Assisted Intervention – MICCAI 2000. Springer, Berlin/Heidelberg, pp. 103–129.
Sherman, R., 2007. Carbon dioxide snow cleaning. Part. Sci. Technol. 25, 37–57.

Singh, R., Lee, P.D., Dashwood, R., Lindley, T., 2010. Titanium foams for biomedical applications: a review. Mater. Technol. 25, 127–136.
Stauber, M., Muller, R., 2008. Micro-computed tomography: a method for the non-destructive evaluation of the three-dimensional structure of biological specimens. In: Westendorf, J.J. (Ed.), Methods in Molecular Biology. Humana Press, Totowa, NJ.
Van Bael, S., Kerckhofs, G., Moesen, M., Pyka, G., Schrooten, J., 2011. Micro-CT-based improvement of geometrical and mechanical controllability of selective laser melted Ti6Al4V porous structures. Mater. Sci. Eng. 528, 7423–7431.
Wadley, H.N.G., 2002. Cellular metals manufacturing. Adv. Eng. Mater. 4, 726–733.
Xue, W., Krishna, B.V., Bandyopadhyay, A., Bose, S., 2007. Processing and biocompatibility evaluation of laser processed porous titanium. Acta Biomater. 3, 1007–1018.
Yue, S., (Thesis) 2011. Non-destructive quantification of tissue scaffolds and augmentation implants using X-ray microtomography. Department of Materials, Imperial College London, London.
Yue, S., Lee, P.D., Poologasundarampillai, G., Jones, J.R., 2011. Evaluation of 3-D bioactive glass scaffolds dissolution in a perfusion flow system with X-ray microtomography. Acta Biomater. 7, 2637–2643.